Synthesis of Compositionally Graded Nanocast NiO/NiCo$_2$O$_4$/Co$_3$O$_4$ Mesoporous Composites with Tunable Magnetic Properties

Moisés Cabo [a], Eva Pellicer [*a], Emma Rossinyol [b], Marta Estrader [c], Alberto López-Ortega [c], Josep Nogués [d], Onofre Castell [b], Santiago Suriñach [a] and Maria Dolors Baró [a]

[a]*Departament de Física, Facultat de Ciències*
Universitat Autònoma de Barcelona
E-08193 Bellaterra (Spain)
E-mail: Eva.Pellicer.icn@uab.cat

[b]*Servei de Microscòpia, Facultat de Ciències*
*Universitat Autònoma de Barcelona*
E-08193 Bellaterra (Spain)

[c]*Centre d'Investigació en Nanociència i Nanotecnologia (ICN-CSIC)*
Campus Universitat Autònoma de Barcelona
E-08193 Bellaterra (Spain)

[d]*Institució Catalana de Recerca i Estudis Avançats (ICREA)*
Centre d'Investigació en Nanociència i Nanotecnologia (ICN-CSIC)
Campus Universitat Autònoma de Barcelona
E-08193 Bellaterra (Spain)

Graphical contents entry

Mesoporous NiO/NiCo$_2$O$_4$/Co$_3$O$_4$ composites showing variable degrees of order and tunable

magnetic properties are achievable by nanocasting using SBA-15 silica as hard templates. The

$NiCo_2O_4$-rich powders are magnetic at room temperature and can be easily remotely manipulated using small fields (see Fig.).
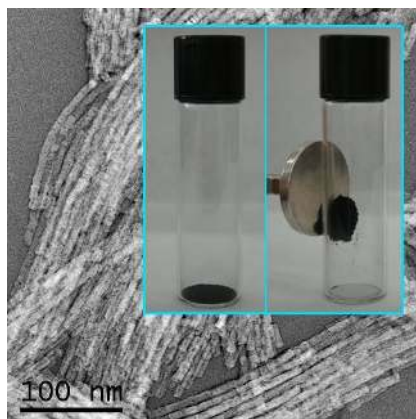
A series of mesoporous $NiO/NiCo_2O_4/Co_3O_4$ composites has been synthesized by nanocasting using SBA-15 silica as a hard template. The evaporation method was used as the impregnation step. Nickel and cobalt nitrates in different Ni(II):Co(II) molar ratios were dissolved in ethanol and used as precursors. The composites show variable degrees of order, from randomly organized nanorods to highly ordered hexagonally-packed nanowires as the Ni(II):Co(II) molar ratio decreases. The materials exhibit moderately large surface areas, in the 60-80 m^2/g range. Their magnetic properties, saturation magnetization (M_S) and coercivity (H_C), can be easily tuned given the ferrimagnetic ($NiCo_2O_4$) and antiferromagnetic (NiO and Co_3O_4) character of the constituents. Moreover, the $NiCo_2O_4$ rich materials are magnetic at room temperature and can consequently be easily manipulated by small magnets. Owing to their appealing combination of properties, the nanocomposites are expected to be attractive for myriad applications.

1. Introduction

The confined growth of solids inside the mesopores of silica matrices within the so-called 'host-guest chemistry' framework has aroused a lot of attention the last decades.[1] Through this approach, many metals and metal oxides either in the form of nanorod, nanowire or nanotube arrays can be fabricated. The 'replicated materials' find potential applications in several fields (optics, magnetics, electronics, catalysis, gas-sensing…) as they combine the physicochemical properties of nonsiliceous materials with the finite-size effects of their nanopores.[2-7] Among the silica compounds available as host, the SBA-15 (*p6mm*) can be regarded as the simplest one owing to its regular 2D porous network constructed by hexagonally arranged straight mesopores connected by some bridging micropores.[8]

To date, several transition metal oxides have been grown inside the channels of SBA-15 silica, and the synthesis of hexagonally-packed nanowire arrays of Cr_2O_3, In_2O_3, Mn_xO_y, Co_3O_4, NiO, Fe_2O_3, CeO_2, and WO_3 has been reported so far.[9-11] Less attention has been paid to the hard-templating of complex oxides (containing two or more types of cations) and composites (combining two or more metal oxides). Very recently, the successful synthesis of mesoporous ferrite and cobaltite spinels has been addressed, thus proving that the 'host-guest' chemistry can be expanded to more complex systems.[12-14] The possibility of producing mesoporous complex oxides and composites is of paramount interest from a fundamental viewpoint since understanding how the interaction between different guests takes place inside the silica channels will lead to a better control of the replicas. From the technological viewpoint, the composites may offer novel applications since one could take advantage of the synergistic effects between the different constituent phases.[15]

Interestingly, nickel and cobalt-based nanomaterials are emerging as ideal candidates in the catalysis field, particularly as low-cost replacements for noble metal catalysts.[16] Mesostructuring is expected to enhance the efficiency of catalytic processes owing to the shape-selective properties and large surface areas of the mesoporous materials.[17,18] Moreover,

the solid solutions of the nickel cobaltite system, denoted as $Ni_{1-x}Co_xO_y$, have exceptionally high activity with regard to the oxygen evolution reaction (OER) in alkaline media.[19] In addition, nanostructured stoichiometric $NiCo_2O_4$ is currently under focus due to its potential technological applications, such as magnetic hyperthermia or electrochemical supercapacitors.[20,21] Hence, the exploitation of the hard-templating possibilities in the synthesis of this class of materials is certainly worthwhile.

In this work we report the hard-template synthesis of compositionally graded $NiO/NiCo_2O_4/Co_3O_4$ composites from SBA-15 silica host as well as their characterization by manifold techniques. The mesoporous composites show variable degrees of order and controllable magnetic response. In particular, the nanocomposites display ferromagnetism at room temperature and can be easily remotely manipulated, thus allowing their use in a broader range of conditions.

2. Results

2.1 Morphological characterization

Fig. 1 shows a set of transmission electron microscopy (TEM) images of different composites obtained by impregnation of SBA-15 silica with nickel and cobalt nitrate precursors (in different proportions), followed by calcination at 550ºC and subsequent template removal. Remarkably, the powders obtained from 1:0 and 0:1 Ni(II):Co(II) molar ratios, i.e. from single precursor, show a rather different morphology (Fig. 1a and 1h). Namely, the cobalt nitrate-derived powder is composed of periodically arranged nanowires, whereas mostly unstuck, short nanorods were formed from the nickel nitrate precursor. This suggests that the small bridges in SBA-15 were not replicated in the same manner. It is in fact known that when the nanobridges are not successfully replicated, short nanorods are obtained instead of a three-dimensional network.[22] Moreover, using a 1:0.11 Ni(II):Co(II) molar ratio, the resulting material is essentially constructed by isolated or randomly organized bundles of few

nanorods (Fig. 1b). Nevertheless, upon increasing the Co(II) amount at the expense of Ni(II), the material becomes progressively more ordered (Fig. 1c-1g). Simultaneously, the nanorods evolve to nanowires, finally rendering large, elongated mesoporous particles composed of hexagonally-arranged nanowires (Fig. 1g). These particles clearly retain the symmetry of the parent 2D hexagonal silica (see Supporting Information, Fig. S1, for TEM images of the SBA-15 silica template).

Fig. 2 shows High Resolution TEM (HRTEM) images of the powders obtained from 1:0, 0.5:1 and 0:1 Ni(II):Co(II) molar ratios. The evolution from defectively connected, twisted nanorods towards straight nanowires is evident as the Co(II) content increases. The nanowires shown in Fig. 2b and 2c have diameters ca. 7.5 nm, while the nanorods in Fig. 2a appear to be thinner in some regions. In all cases, lattice fringes are observed in the TEM images, revealing the high crystallinity of the powders. In Fig. 2a the 2.4 Å periodicity of the observed fringes is compatible with the distance expected between the (111) planes of face-centered cubic NiO (JCPDF 73-1519). The fringes in Fig. 2b can be assigned to the (111), (220), (311) and (400) (4.7 Å, 2.8 Å, 2.4 Å and 2.0 Å respectively) reflections of $NiCo_2O_4$ spinel (JCPDF 73-1702). Analogously, the fringes in Fig. 2c are assigned to the Co_3O_4 spinel (JCPDF 71-0816). Note also that different wires show different growth orientations, implying that the confined growth does not determine the growth direction.

2.2 Structural characterization

In order to further corroborate the dependence of the degree of order on the Ni(II):Co(II) molar ratio, low-angle X-ray diffraction (XRD) patterns were acquired. Fig. 3 shows the low-angle region of the SBA-15 silica host along with the templated materials after silica removal. The former exhibits three well-resolved peaks associated with the (100), (110) and (200) reflections of the *p6mm* hexagonal symmetry demonstrating its high degree of order.[8] For the replicated materials, the detection of the characteristic mesostructure reflections is clearly

linked to the Ni(II):Co(II) molar ratio. As this ratio is decreased below 1:1, the low-angle reflections begin to appear, indicating the formation of ordered domains.[23] This clearly confirms that the degree of order depends markedly on the Ni(II):Co(II) molar ratio, in agreement with TEM observations.

The wide-angle XRD patterns of the synthesized powders, plotted in a 3D graph, are shown in Fig. 4a. Broad reflections were observed in all patterns, indicating the existence of nanocrystalline phases. Successful removal of the silica template was assessed from the absence of a wide reflection at around $2\theta = 25^\circ$. In fact, silicon was not detected by energy dispersive X-ray analyses (EDS) performed in the TEM either. Table 1 lists the cell parameter, a, crystallite size, $<D>$, and phase amount (in wt%) extracted from the Rietveld refinement of the XRD patterns. The diffactograms in green and red color belong to the materials obtained from single precursor and are assigned to cubic NiO and Co_3O_4 phases, respectively. Within the range where mixed precursors were used, i.e. 1:0.11-0.11:1 Ni(II):Co(II) molar ratios, either two or three phases coexisted. With decreasing the nickel nitrate precursor amount in the synthesis, the XRD patterns show the presence of NiO together with $NiCo_2O_4$ spinel phase. As can be seen in Fig. 4b, the amount of nickel cobaltite progressively increases at the expense of NiO up to a maximum of about 97 wt%, which corresponds to the nominal molar ratio (0.5:1) theoretically needed to obtain the stoichiometric $NiCo_2O_4$ spinel (see pattern in blue). However, the pure $NiCo_2O_4$ phase is not formed, but a nickel-deficient off-stoichiometric $NiCo_2O_4$ phase accompanied by NiO impurities is obtained. With decreasing further the amount of nickel nitrate precursor beyond the 0.5:1 Ni(II):Co(II) ratio towards the 0.11:1 ratio, the XRD patterns show the presence of an additional phase (Co_3O_4). The amount of Co_3O_4 increases while the $NiCo_2O_4$ one falls (see Fig. 4b and Table 1) as the Ni precursor is reduced. Nevertheless, the presence of NiO is still detected even for low Ni(II) contents (e.g., in Fig. S2 the XRD pattern corresponding to the 0.25:1 Ni(II):Co(II) molar ratio is shown, where the NiO peaks are indicated). Note that discriminating between the $NiCo_2O_4$

and Co_3O_4 phases, both of which have a spinel structure, is not straightforward. Their XRD patterns are almost identical and the close inspection of high angle reflections is necessary to assess the presence of Co_3O_4. At this point it should be emphasized that the extracted phase weight amounts should not be taken quantitatively, but from a qualitative viewpoint. The Rietveld analysis of a multi phase sample is an extremely complex refinement process and the weight fraction is strongly correlated with the most of the refined parameters. However, the obtained values are fully consistent with the magnetic response displayed by the powders as it will be shown later. The lattice parameter of the spinel $NiCo_2O_4$ deviates from the bulk lattice constant ($a = 8.114$ Å) (Table 1). It should be kept in mind that the $NiCo_2O_4$ phase is probably nickel-deficient, that is, slightly out of the ideal stoichiometry, since some NiO segregates from the spinel during the calcination step.[14] Partial decomposition of the spinel into NiO is known to occur above 400−500 °C.[24] This feature could in fact contribute to the observed cell parameter values. The lattice constants of both NiO and Co_3O_4 also deviate from their bulk values (4.168 Å and 8.065 Å, respectively).

Interestingly, the Brunauer-Emmett-Teller (BET) analyses show that moderately large surface areas are obtained independently of the replica morphology. For example, pure NiO and Co_3O_4 powders have BET surface areas of about 74 m^2/g and 64 m^2/g, respectively. These values are close to the ones reported in the literature for hard-templated nickel and cobalt oxides and would justify their use in catalysis applications.[25,26] Meanwhile, the $NiCo_2O_4$/NiO composite derived from the 0.5:1 Ni(II):Co(II) molar ratio, thus having the maximum $NiCo_2O_4$ amount, exhibited a BET surface area of 81 m^2/g, which also compares nicely with mesoporous $NiCo_2O_4$ synthesized by one-step nanocasting as well as aerogels produced by sol-gel routes.[19,27] Typical isotherms are shown in Figure S3 (Supporting Information). Importantly, the multi-step nanocasting approach has the advantage that it overcomes the structural instability encountered in soft-chemistry approaches and does not require specific equipment such as supercritical dryers commonly employed in aerogel synthesis.

In order to clarify the origin of the correlation between the degree of order and the different precursors, thermogravimetric analyses (TGA) of the metal nitrate salts were carried out. Fig. 5 shows the TGA mass/temperature curves of nickel nitrate, cobalt nitrate and a mixture of metal nitrates in 0.5:1 Ni(II):Co(II) molar ratio. It can be seen that the different steps, i.e., loss of adsorbed water, further decomposition of the nitrates and final oxide crystallization, occur at lower temperature for cobalt nitrate compared to nickel nitrate. On the other hand, decomposition/crystallization of the mixed nitrates, from which the $NiCo_2O_4$ spinel is mainly formed, occurs at intermediate temperatures. It is thus likely that the growth of the different constituents (NiO, Co_3O_4 and $NiCo_2O_4$) in the silica channels during calcination takes place at different temperatures and therefore, on different time scales. This would severely hinder the growth of long wires especially in the case of the $NiO/NiCo_2O_4$ composites. Since the $NiCo_2O_4$ phase forms at lower temperature compared to NiO, this results in the formation of discontinuous nanorods due to an inhomogeneous material growth. Upon dissolution of the silica template, the short nanorods are not able to keep the self-supported periodic arrangement. The same behaviour was observed for impregnated silica (i.e. when performing the thermal analyses of the metal nitrates inside the silica pores). As shown schematically in Fig. 6a inhomogeneous oxide growth inside the silica template leads to nanorods after silica removal, whereas continuous filling generates the mesoporous replica (Fig. 6b). Within the $NiO/NiCo_2O_4$ series, such effect becomes more pronounced as the Ni(II):Co(II) molar ratio increases, highlighting the fact that the interaction between different guests determines the final morphology of the replicas.

2.3 Magnetic properties

Fig. 7 shows that the combination of ferrimagnetic (FiM) and antiferromagnetic (AFM) phases allows for a tuning of both the saturation magnetization, M_S, and the coercivity, H_C, of the composites. First of all, it should be stressed that the response of mesoporous pure Co_3O_4

is typical of an AFM material, in which the magnetization increases almost linearly with the magnetic field, while the AFM NiO powder displays a hysteresis loop that can be understood on the basis of finite size effects well described for NiO nanoparticles.[28] These results are consistent with studies of mesoporous NiO and Co_3O_4.[29-31] The presence of $NiCo_2O_4$ spinel phase in the composites gives rise to clear hysteresis loops owing to its FiM nature.

The experimental magnetization has been found not to saturate even at the maximum applied field (70 kOe), as expected from the contribution of AFM phases and magnetic surface disorder effects often observed at reduced dimensions.[32,33] The M_S obtained after subtracting the linear contribution, increases with the amount of $NiCo_2O_4$ (Table 2), which confirms that this compound definitely forms instead of, for example, a NiO-Co_3O_4 solid solution. The increase of M_S with the amount of $NiCo_2O_4$ spinel is in agreement with the refined phase percentage estimated by means of XRD. The composite with the highest $NiCo_2O_4$ spinel amount (97 wt%) has M_S of 24 emu/g, slightly lower than in mesoporous pure $NiCo_2O_4$ (26 emu/g)[14] and bulk $NiCo_2O_4$ (29 emu/g).[34] Remarkably, the high field susceptibility of the loops depends significantly on the composition of the material, being larger for composites containing Co_3O_4. This is likely caused by the difference in AFM susceptibility between NiO and Co_3O_4 (see Fig. 7). This demonstrates that magnetic measurements are a powerful fingerprint of the presence of phases with dissimilar magnetic properties in the composites. Importantly, the coercivity exhibits a non-monotonic behaviour, reaching values in excess of H_C = 1600 Oe for composites containing similar amounts of NiO and $NiCo_2O_4$ (see Table 2). Due to the morphology and composition of these materials, H_C is likely to have two main contributions apart from magnetocrystalline anisotropy: shape anisotropy and AFM-FiM exchange coupling. As the material transforms from nanorods to nanowires, their shape anisotropy increase significantly leading to an increase in coercivity.[35,36] Moreover, when FiM materials are exchange coupled to AFMs and the latter has a low anisotropy (like in the case of NiO) the FiM has to drag the spins of the AFM during the reversal which costs an

extra energy resulting in an increased H_C. Since this is an interface effect, the amount of AFM material and the degree of coupling determine the coercivity enhancement.[37,38] Moreover, FiM materials are known to have magnetic disorder at the surface, which depends on the shape, that also contributes to H_C at low temperatures.[37,39]

Interestingly, the composites are still FiM at room temperature (Fig. 8), i.e., the superparamagnetic blocking temperature, T_B, is higher than 300 K. In particular, the composites rich in $NiCo_2O_4$ exhibit M_S in the range of $M_S \sim$ 2-3.5 emu/g and moderate coercivities $H_C \sim$ 50-300 Oe. In spite of the fact that the bulk Curie temperature of $NiCo_2O_4$ is well above room temperature (T_C = 500 ºC),[33] the magnetic stability of the composites at room temperature is somewhat surprising, given the small volume, V, and the rather low anisotropy, K, of $NiCo_2O_4$[24] (since $T_B = KV/25k_B$,[40] where k_B is the Boltzman constant). Probably the enhanced T_B is due to an increased of the effective anisotropy due to the shape anisotropy[36] and the FiM-AFM exchange coupling.[41]

The room temperature FiM character of the samples results in another appealing effect. Namely, the powders are strongly attracted to a small tabletop magnet (see Fig. 9) and can consequently be easily manipulated using small fields. This opens new perspectives for applications of these materials since by using magnetic fields they can be moved to or trapped in specific locations where the desired application wants to be implemented.

3. Conclusions

Nickel- and cobalt-based mesoporous composites have been prepared by nanocasting from SBA-15 silica templates. Depending on the Ni(II):Co(II) molar ratio of the precursors, the nanocast $NiO/NiCo_2O_4/Co_3O_4$ composites show distinct morphology and order, from disordered nanorods at high ratios to hexagonally-packed nanowires at low ratios. The materials are ferrimagnetic at low temperatures with a maximum M_S of 24 emu/g (for the

sample with 97 wt% of $NiCo_2O_4$) and $H_C > 1600$ Oe (for the sample containing 53 wt% of $NiCo_2O_4$). The combination of FiM and AFM phases allowed for a fine tuning of the magnetic properties. Moreover, the synthesized nanocomposites are ferromagnetic at room temperature and can be easily manipulated using small fields. Applications of these hybrid materials, which have been largely overlooked in the past, are expected to grow in the near future by virtue of the interesting properties derived from the nanoscaling.

4. Experimental Section

Unless stated, chemicals used in all syntheses were purchased from Sigma-Aldrich and used without further purification. Reagent-grade (Milli-Q) water was also used.

Mesoporous silica SBA-15 was synthesized by dissolving 6.0 g of Pluronic P123 copolymer (BASF corporation) in diluted HCl. Tetraethyl ortosilicate (12.5 g), which served as the silicon source, was then added and the solution stirred for 24 h at a constant temperature (about 37 ºC). The hydrothermal treatment was carried out at 90 ºC in a sealed container and the solid obtained was filtered, copiously washed with water and finally calcined at 550 ºC for 5 h to remove the organic surfactants.

For the synthesis of the replicas, 0.150 g of mesoporous silica template was mixed with x g of $Ni(NO_3)_2 \cdot 6H_2O$ plus $(0.291 - x)$ g of $Co(NO_3)_2 \cdot 6H_2O$ (99.999% purity) dissolved in ethanol. The total metal nitrate amount was kept at 1 mmol. The Ni(II):Co(II) molar ratio was varied as follows: 1:0, 1:0.11, 1:0.25, 1:0.43, 1:0.67, 1:1, 0.67:1, 0.5:1, 0.25:1, 0.11:1, 0:1. The mixtures were stirred for 30 min in a crucible and left for ethanol evaporation overnight. The crucible was then placed in a tubular furnace and the impregnated silica was calcined. The furnace temperature was increased to 550 ºC at a rate of 3 ºC/min and held at this temperature for 4 h in air. At the end of this process, the furnace was slowly cooled down to room temperature. Note that calcination at 550ºC leads to an increased thermal stability of the porous network compared to treatments at lower temperatures.[14] The silica matrix was

removed with 30 mL of 2 M NaOH solution at 70 ºC under stirring. The powder was collected after centrifugation and decanted off the supernatant, copiously rinsed in absolute ethanol and finally dried in vacuum. The formation of metal oxides from metal nitrates was quantitative in all cases.

The synthesized composites were characterized by transmission electron microscopy (TEM), X-ray diffraction (XRD), Brunauer-Emmett-Teller method (BET) surface area analysis, and magnetic measurements. TEM characterization was performed on a Jeol-JEM 2011 microscope operated at 200 kV. The samples for TEM were prepared by dispersing a small amount of the powder in ethanol and then one or two drops of the suspension were deposited onto a holey carbon supported grid. Low-angle XRD patterns were recorded on a Panalytical X'Pert Pro diffractometer operating in transmission mode with Cu Kα radiation. Wide-angle XRD patterns were collected on a Phillips X'Pert diffractometer in the 15-90º 2θ range using Cu Kα radiation. The structural parameters were evaluated by fitting the XRD patterns over the entire measured profile using the 'Materials Analysis Using Diffraction' (MAUD) Rietveld refinement program.[42,43] BET analyses were performed on a Micromeritics ASAP 2020 accelerated surface area and porosimetry analyzer. The magnetic properties were studied by measuring hysteresis loops at low and room temperatures using a MPMS-XL7 Superconducting Quantum Interference device (SQUID) and a vibrating sample magnetometer (VSM) from Oxford Instruments, respectively. The SQUID hysteresis loops were recorded in the ±70 kOe range at 10 K after zero-field-cooling (ZFC) from room temperature. Thermogravimetric Analysis (TGA) of the metal nitrate precursors was carried out using a Perkin Elmer TGA7 equipment. The nitrate salts were placed in an alumina crucible and heated from ambient temperature to 550 ºC in air (flow rate 20 mL/min; heating rate 10 °C/min).

Acknowledgements

[1]   Y. Wan, H. Yang and D. Zhao, *Acc. Chem. Res.* 2006, **39**, 423-432.

[2]   Q. Lu, Z. Wang, J. Li, P. Wang and X. Ye, *Nanoscale Res. Lett.* 2009, **4**, 646-654.

[3]   H. Tüysüz, M. Comotti and F. Schüth, *Chem. Commun.* 2008, 4022-4024.

[4]   Z. Li, C. Kübel, V. I. Pârvulescu and R. Richards, *ACS Nano* 2008, **2**, 1205-1212.

[5]   A. Prim, E. Pellicer, E. Rossinyol, F. Peiró, A. Cornet and J. R. Morante, *Adv. Funct. Mater.* 2007, **17**, 2957-2963.

[6]   F. Jiao, A. Harrison, J.-C. Jumas, A. V. Chadwick, W. Kockelmann and P. G. Bruce, *J. Am. Chem. Soc.* 2006, **128**, 5468-5474.

[7]   I. V. Golosovky, I. Mirebeau, V. P. Sakhnenko, D. A. Kurdyukov and Y. A. Kumzerov, *Phys. Rev. B* 2005, **72**, 144409.

[8]   D. Zhao, J. Feng, Q. Huo, N. Melosh, G. H. Fredrickson, B. F. Chmelka and G. D. Stucky, *Science* 1998, **279**, 548-552.

[9]   M. Tiemann, *Chem. Mater.* 2008, **20**, 961-971.

[10]   I. Lopes, N. El Hassan, H. Guerba, G. Wallez and A. Davidson, *Chem. Mater.* 2006, **18**, 5826-5828.

[11]   W. Yue and W. Zhou, *Chem. Mater.* 2007, **19**, 2359-2363.

[12]   J. Zhu and Q. Gao, *Micro. Meso. Mater.* 2009, **124**, 144-152.

[13]   M. Gu, B. Yue, R. Bao and H. He, *Mater. Res. Bull.* 2009, **44**, 1422-1427.

[14]   M. Cabo, E. Pellicer, E. Rossinyol, O. Castell, S. Suriñach and M. D. Baró, *Cryst. Growth Des.* 2009, **9**, 4814-4821.

[15]   M. M. Natile and A. Glisenti, *Chem. Mater.* 2003, **15**, 2502-2510.

[16]   P. Boldrin, A. K. Hebb, A. A. Chaudhry, L. Otley, B. Thiebaut, P. Bishop and J. A. Darr, *Ind. Eng. Chem. Res.* 2007, **46**, 4830-4838.

[17]   Z.-R. Tian, W. Tong, J.-Y. Wang, N.-G. Duan, V. V. Krishnan, S. L. Suib, *Science* 1997, **276**, 926-930.

[18]   Y. Rao, D. M. Antonelli, *J. Mater. Chem.* 2009, **19**, 1937-1944.

[19]   R. N. Singh, J. P. Pandey, N. K. Singh, B. Lal, P. Chartier and J.-F. Koenig, *Electrochim. Acta* 2000, **45**, 1911-1919.

[20]   S. Verma, H. M. Joshi, T. Jagadale, A. Chawla, R. Chandra and S. Ogale, *J. Phys. Chem. C* 2008, **112**, 15106-15112.

[21]   T.-Y. Wei, C.-H. Chen, H.-C. Chien, S.-Y. Lu and C.-C. Hu, *Adv. Mater.* 2010, **22**, 347-351.

[22]   K. Zhu, H. He, S. Xie, X. Zhang, W. Zhou, S. Jin and B. Yue, *Chem. Phys. Lett.* 2004, **377**, 317-321.

[23]   A. Rumplecker, F. Kleitz, E.-L. Salabas, F. Schüth, *Chem. Mater.* 2007, **19**, 485-496.

[24]   Y. Kobayashi, X. Ke, H. Hata, P. Schiffer and T. E. Mallouk, *Chem. Mater.* 2008, **20**, 2374-2381.

[25]   K. M. Shaju, F. Jiao, A. Débart and P. G. Bruce, *Phys. Chem. Chem. Phys.* 2007, **9**, 1837-1842.

[26]   Y.-G. Wang and Y.-Y. Xia, *Electrochim. Acta* 2006, **51**, 3223-3227.

[27]   M. A. Carreon, V. V. Guliants, L. Yuan, A. R. Hughett, A. Dozier, G. A. Seisenbaeva and V. G. Kessler, *Eur. J. Inorg. Chem.* 2006, **24**, 4983-4988.

[28]   R. H. Kodama, S. A. Makhlouf and A. E. Berkowitz, *Phys. Rev. Lett.* 1997, **79**, 1393-1396.

[29]   Y. Wang, C.-M. Yang, W. Schmidt, B. Spliethoff, E. Bill and F Schüth, *Adv. Mater.* 2005, **17**, 53-56.

[30]   W. Yue, A. H. Hill, A. Harrison and W. Zhou, *Chem. Commun.* 2007, 2518-2520.

[31]   F. Jiao, A. H. Hill, A. Harrison, A. Berko, A. V. Chadwick and P. G. Bruce, *J. Am. Chem. Soc.* 2008, **130**, 5262-5266.

[32]   X. Batlle and A. Labarta, *J. Phys. D: Appl. Phys.* 2002, **35**, R15-R42.

[33]   S. Mørup, D. E. Madsen, C. Frandsen, C. R. H. Bahl and M. F. Hansen, *J. Phys. Condens. Matter* 2007, **19**, 213202.

[34]   O. Knop, K. I. G. Reid, Sutarno and Y. Nakagawa, *Can. J. Chem.* 1968, **46**, 3463-3476.

[35]   R. Skomski, *J. Phys. Condens. Matter* 2003, **15**, R841-R896.

[36]   J. I. Martín, J. Nogués, K. Liu, J. L. Vicent and I. K. Schuller, *J. Magn. Magn. Mater.* 2003, **256**, 449-501.

[37]   J. Nogués, J. Sort, V. Langlais, V. Skumryev, S. Suriñach, J. S. Muñoz and M. D. Baró, *Phys. Rep.* 2005, **422**, 65-117.

[38]   J. Sort, J. Nogués, X. Amils, S. Suriñach, J. S. Muñoz and M. D. Baró, *Appl. Phys. Lett.* 1999, **75**, 3177-3179.

[39]   G. Salazar-Alvarez, J. Qin, V. Sepelák, I. Bergmann, M. Vasilakaki, K. N. Trohidou, J. D. Ardisson, W. A. A. Macedo, M. Mikhaylova, M. Muhammed, M. D. Baró and J. Nogués, *J. Am. Chem. Soc.* 2008, **130**, 13234-13239.

[40]   M. Knobel, W. C. Nunes, L. M. Socolovsky, E. De Biasi, J. M. Vargas and J. C. Denardin, *J. Nanosci. Nanotechnol.* 2008, **8**, 2836-2857.

[41]   V. Skumryev, S. Stoyanov, Y. Zhang, G. Hadjipanayis, D. Givord and J. Nogués, *Nature* 2003, **423**, 850-853.

[42]   M. Morales, D. Chateigner and L. Lutterotti, *Thin Solid Films* 2009, **517**, 6264-6270.

[43]   http://www.ing.unitn.it/~maud/
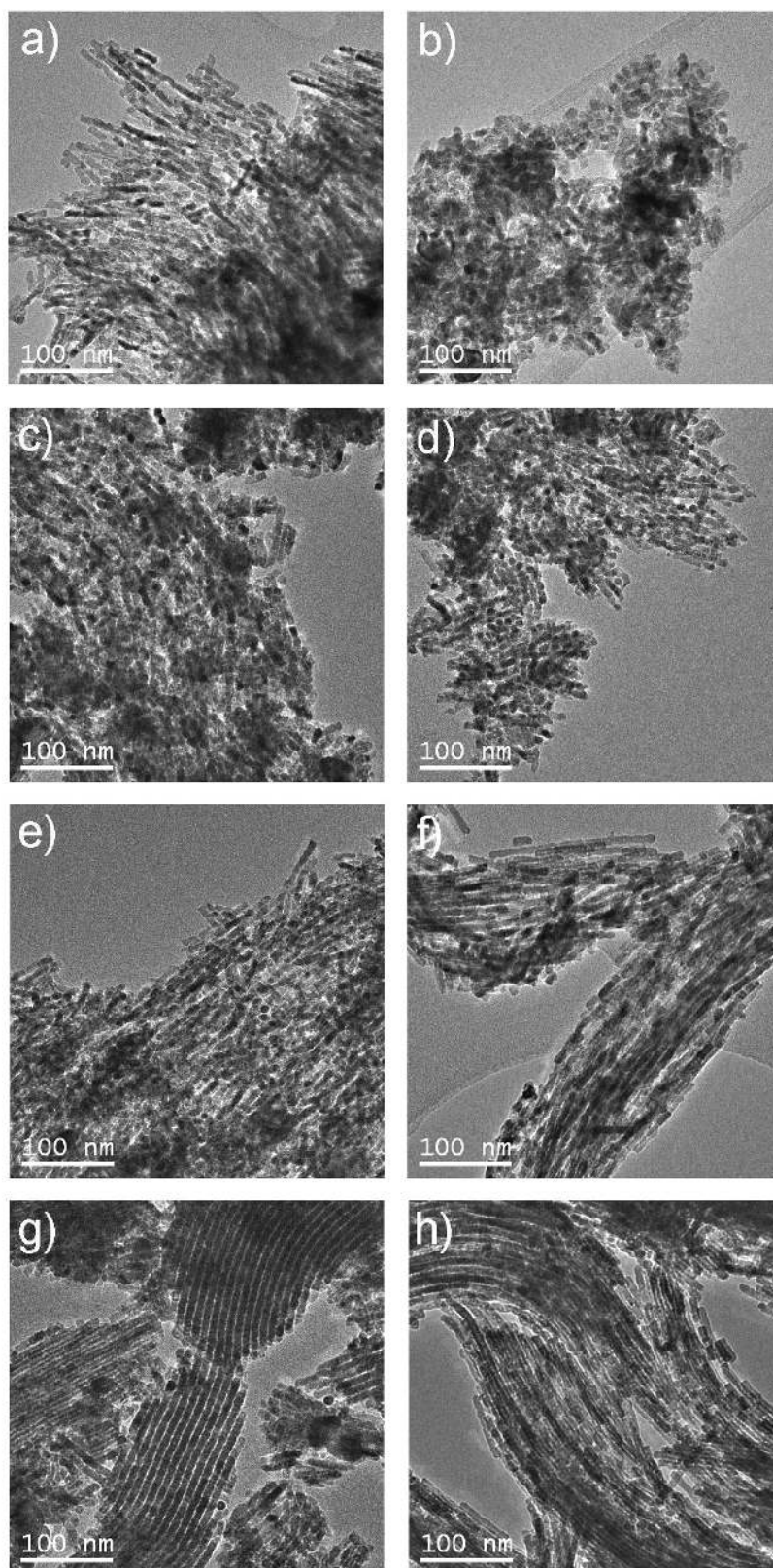
Fig. 1. TEM images of powders synthesized using different Ni(II):Co(II) molar ratios: a) 1:0, b) 1:0.11, c) 1:0.67, d) 1:1, e) 0.67:1, f) 0.25:1, g) 0.11:1 and h) 0:1.
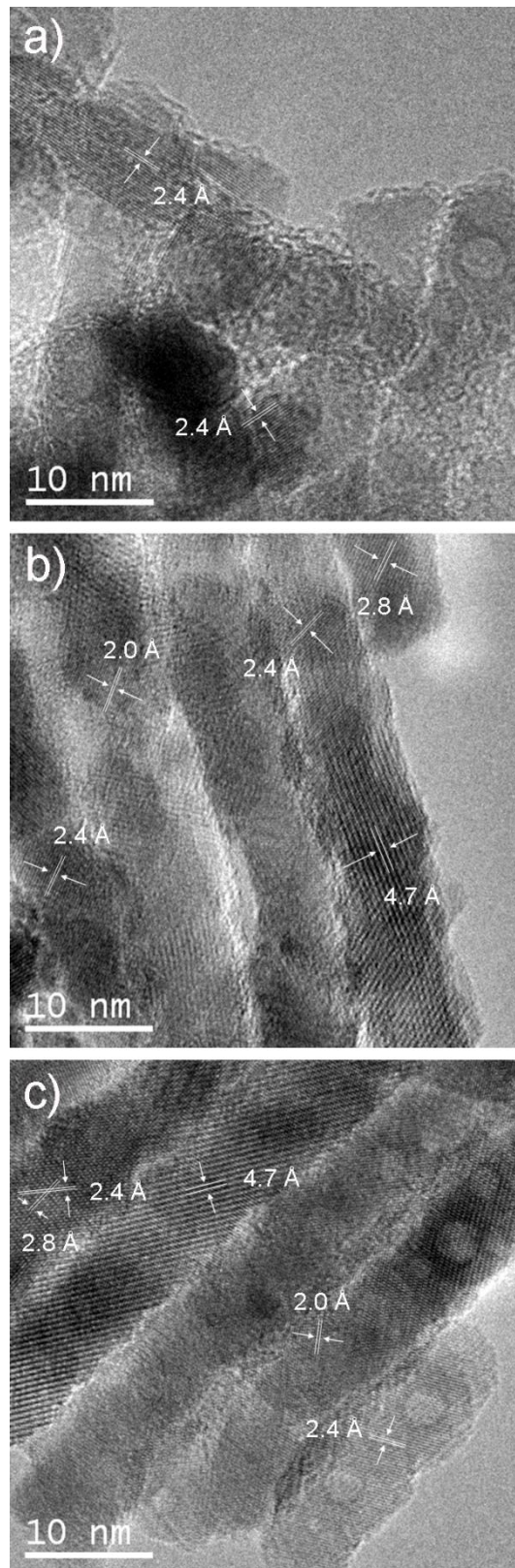
Fig. 2. HRTEM images of powders synthesized using a) 1:0, b) 0.5:1 and c) 0:1 Ni(II):Co(II)

molar ratios. The marked interplanar distances belong to a) face-centered cubic NiO, b)

$NiCo_2O_4$ spinel and c) Co_3O_4 spinel.
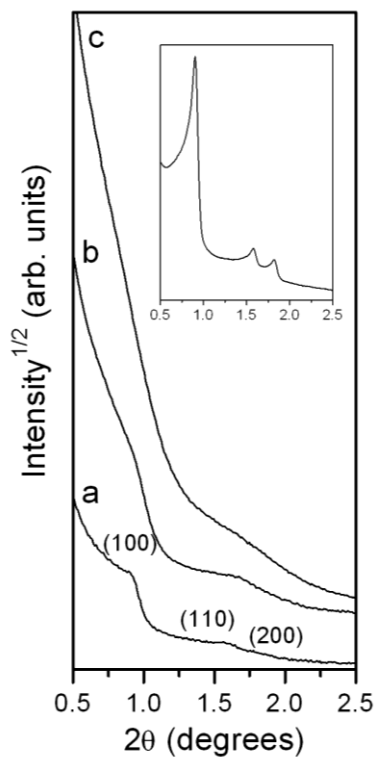
Fig. 3. Low-angle XRD patterns of nanocast powders obtained from a) 0.11:1 , b) 0.25:1, and c) 0.67:1 Ni(II):Co(II) molar ratios. The inset shows the low-angle XRD pattern of SBA-15 silica template.
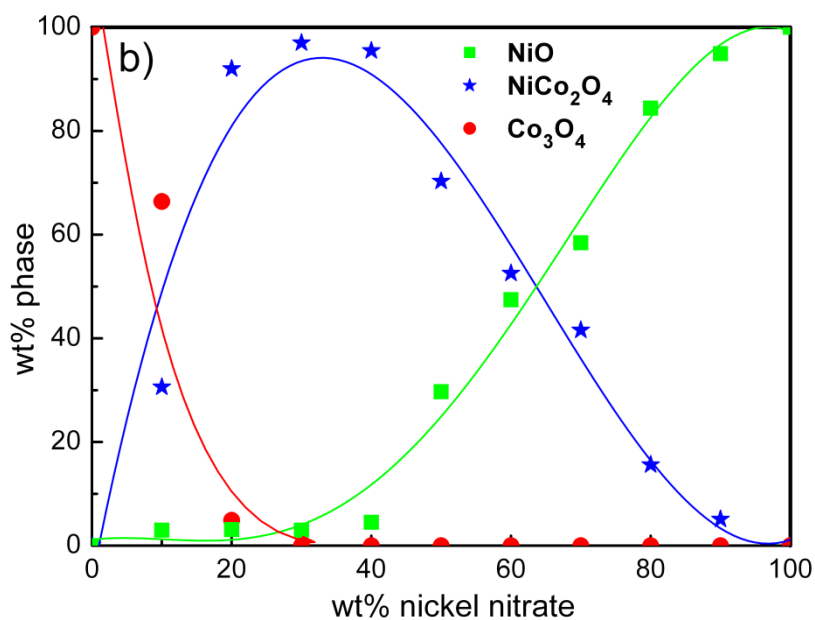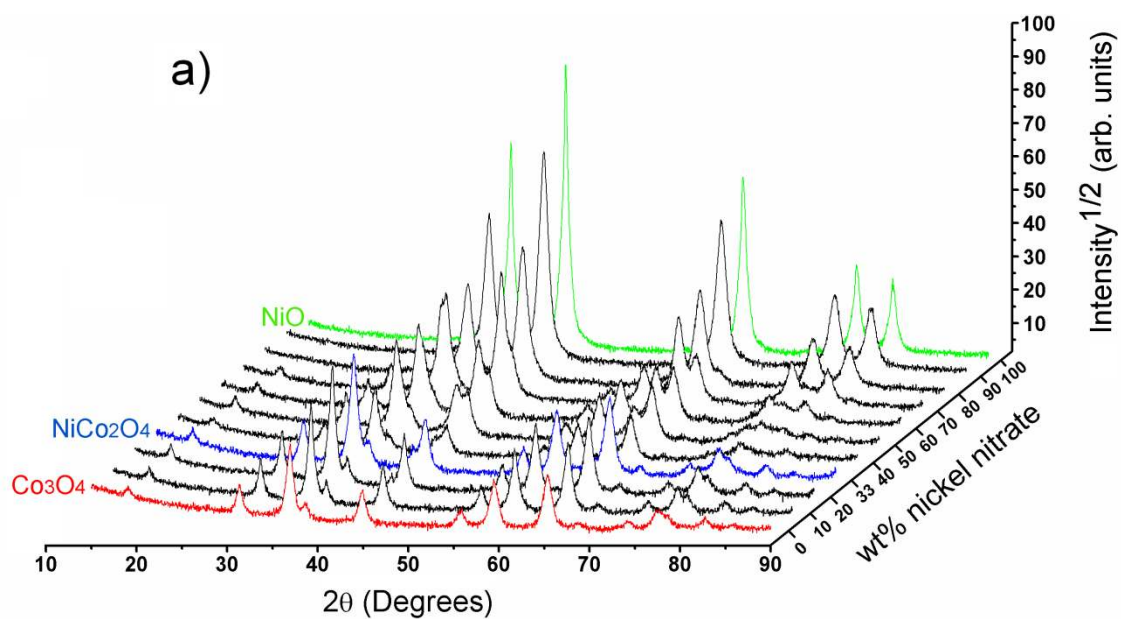
Fig. 4. a) XRD patterns of the synthesized powders. The patterns are shifted along the z-axis, which corresponds to the amount of nickel nitrate precursor used in the synthesis. For clarity, the patterns of pure NiO, almost pure $NiCo_2O_4$ and pure Co_3O_4 are in green, blue and red colors respectively. b) Variation of the refined phase percentages as a function of the nickel nitrate amount used in the synthesis. The solid lines are an eye-guide.

Table 1. Cell parameter (*a*), crystallize size (⟨*D*⟩) and phase amount (wt%) values extracted from Rietveld refinement of the full XRD patterns. <mark>The standard deviations from the refinements are given in brackets.</mark>

Ni(II):Co(II) molar ratio	wt% nickel nitrate	NiO (*Fm3m*)			NiCo$_2$O$_4$ (*Fd3m*)			Co$_3$O$_4$ (*F43m*)		
		a ($\pm5 \times 10^{-3}$ Å)	⟨D⟩ (±5 nm)	wt% (±5)	*a* ($\pm5 \times 10^{-3}$ Å)	⟨D⟩ (±5 nm)	wt% (±5)	*a* ($\pm5 \times 10^{-3}$ Å)	⟨D⟩ (±5 nm)	wt% (±5)
1:0	100	4.177	22	100	--	--	--	--	--	--
1:0.11	90	4.177	18	95	8.135	11	5	--	--	--
1:0.25	80	4.172	14	84	8.132	11	16	--	--	--
1:0.43	70	4.177	13	58	8.129	13	42	--	--	--
1:0.67	60	4.183	13	47	8.143	16	53	--	--	--
1:1	50	4.179	12	30	8.142	15	70	--	--	--
0.67:1	40	4.166	19	5	8.130	17	95	--	--	--
0.5:1	33	4.177	11	3	8.124	17	97	--	--	--
0.25:1	20	4.182	15	3	8.113	22	92	8.091	34	5
0.11:1	10	4.182	22	3	8.102	25	31	8.077	26	66
0:1	0	--	--	--	--	--	--	8.070	21	100
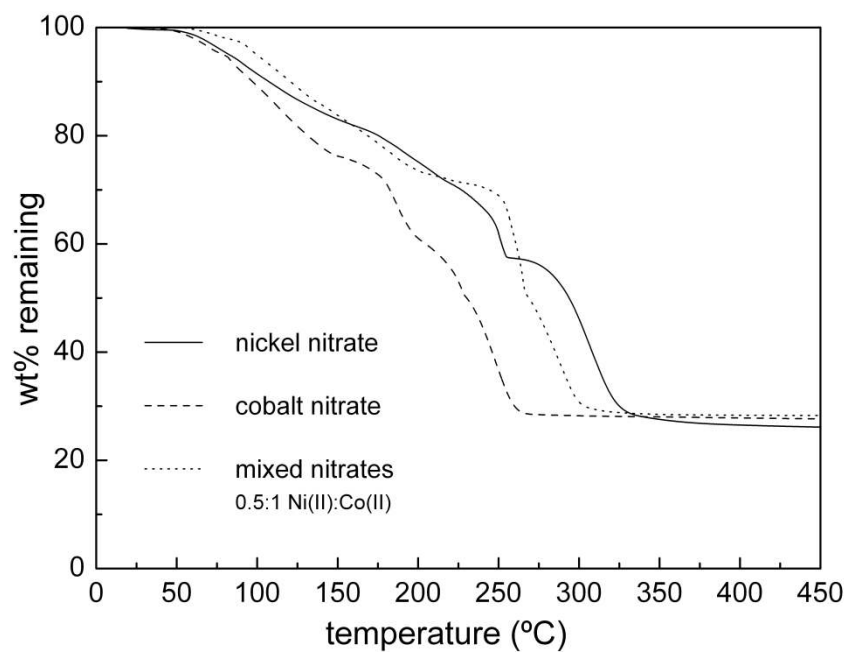
Fig. 5. TGA curves of $Ni(NO_3)_2\cdot6H_2O$, $Co(NO_3)_2\cdot6H_2O$ and a mixture of these nitrates in 0.5:1 Ni(II):Co(II) molar ratio.
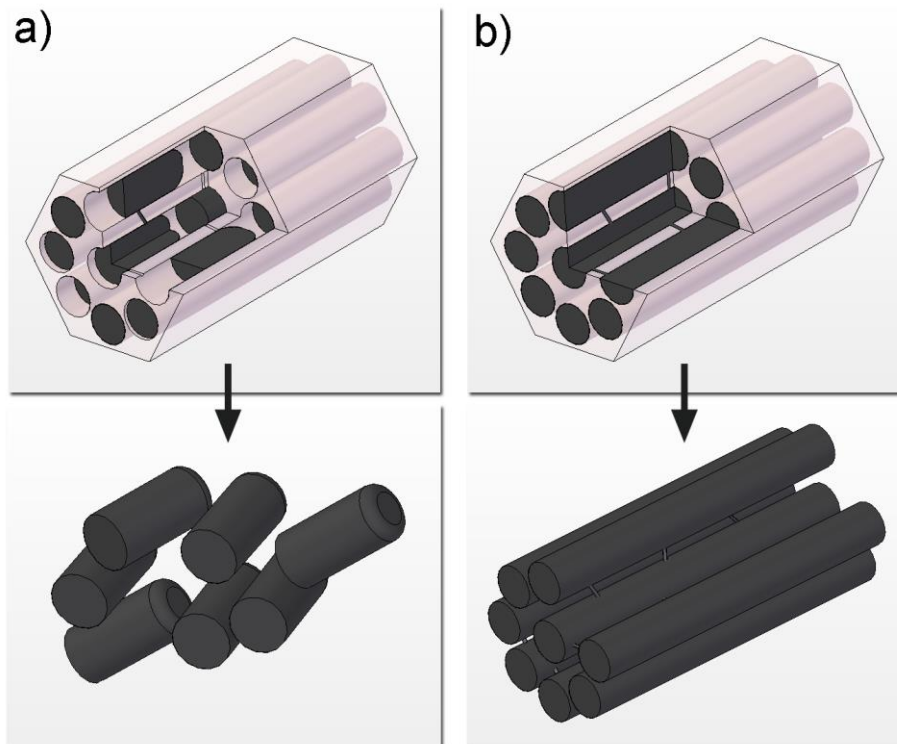
Fig. 6. Schematic picture of material crystallization inside the SBA-15 silica matrix and the morphology resulting after silica removal in the case of a) inhomogeneous and b) complete filling of the silica channels.
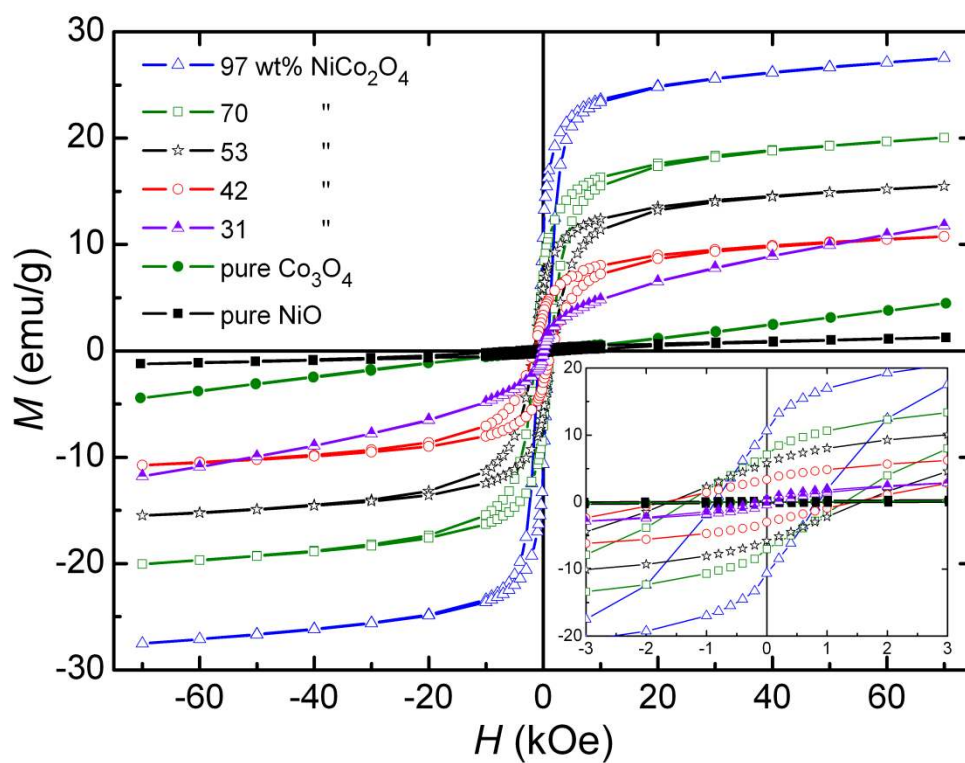
Fig. 7. Hysteresis loops at 10K of various composites (the corresponding refined NiCo₂O₄ phase percentages are given in the left side) together with pure Co₃O₄ and NiO. An enlarged view at low fields is shown in the inset.

Table 2. M_S and H_C values extracted from the hysteresis loops at 10K of the synthesized powders after subtracting the high-field linear contribution.

wt% nickel nitrate	Phases present	M_S (emu/g)	H_C (Oe)
100	NiO*	0.5	4032
90	95 wt% NiO / 5 wt% $NiCo_2O_4$	1	215
80	84 wt% NiO / 16 wt% $NiCo_2O_4$	2	918
70	58 wt% NiO / 42 wt% $NiCo_2O_4$*	9	1596
60	47 wt% NiO / 53 wt% $NiCo_2O_4$*	13	1608
50	30 wt% NiO / 70 wt% $NiCo_2O_4$*	17	1308
40	5 wt% NiO / 95 wt% $NiCo_2O_4$	22	981
33	3 wt% NiO/ 97 wt% $NiCo_2O_4$*	24	860
20	3 wt% NiO / 92 wt% $NiCo_2O_4$ / 5 wt% Co_3O_4	19	429
10	3 wt% NiO / 31 wt% $NiCo_2O_4$ / 66 wt% Co_3O_4*	5	169
0	Co_3O_4*	--	--

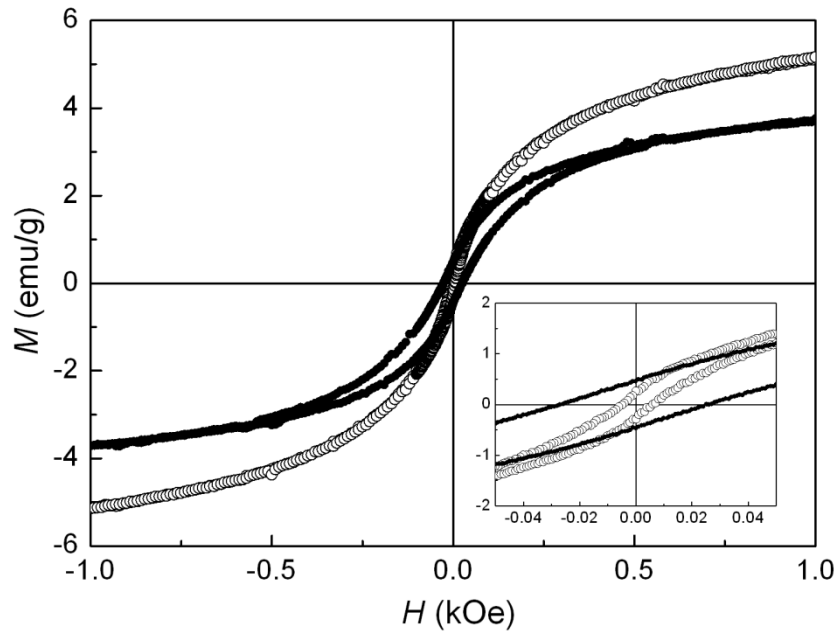*The corresponding loops are displayed in Fig. 7.

Fig. 8. Room temperature hysteresis loops of the composites with 95 wt% (o) and 53 wt% (•) NiCo$_2$O$_4$ spinel. An enlarged view at low fields is shown in the inset.
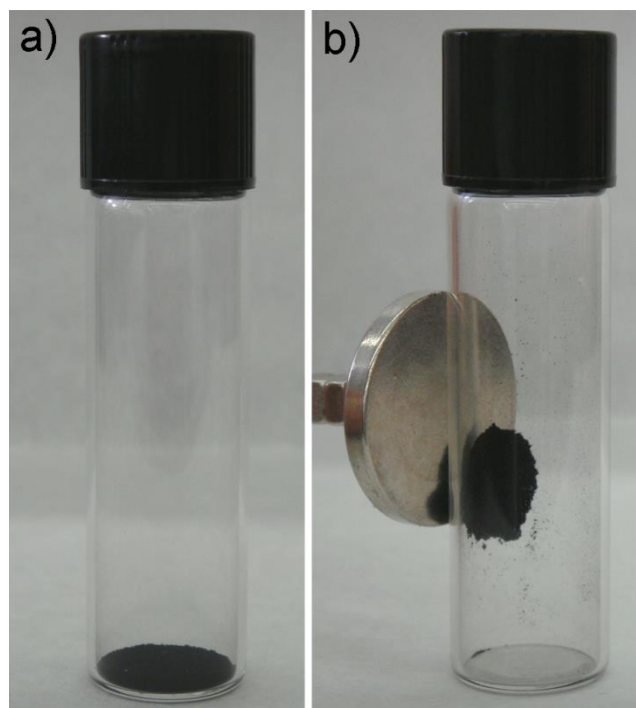
Fig. 9. Photos showing a) the blackish powder corresponding to the nanocomposite with 95 wt% NiCo$_2$O$_4$ and b) the powder being strongly attracted to the magnet when this is brought near the vial.

Synthesis of Compositionally Graded Nanocast NiO/NiCo$_2$O$_4$/Co$_3$O$_4$ Mesoporous Composites with Tunable Magnetic Properties

Moisés Cabo, Eva Pellicer, Emma Rossinyol, Marta Estrader, Alberto López-Ortega, Josep Nogués, Onofre Castell, Santiago Suriñach and Maria Dolors Baró
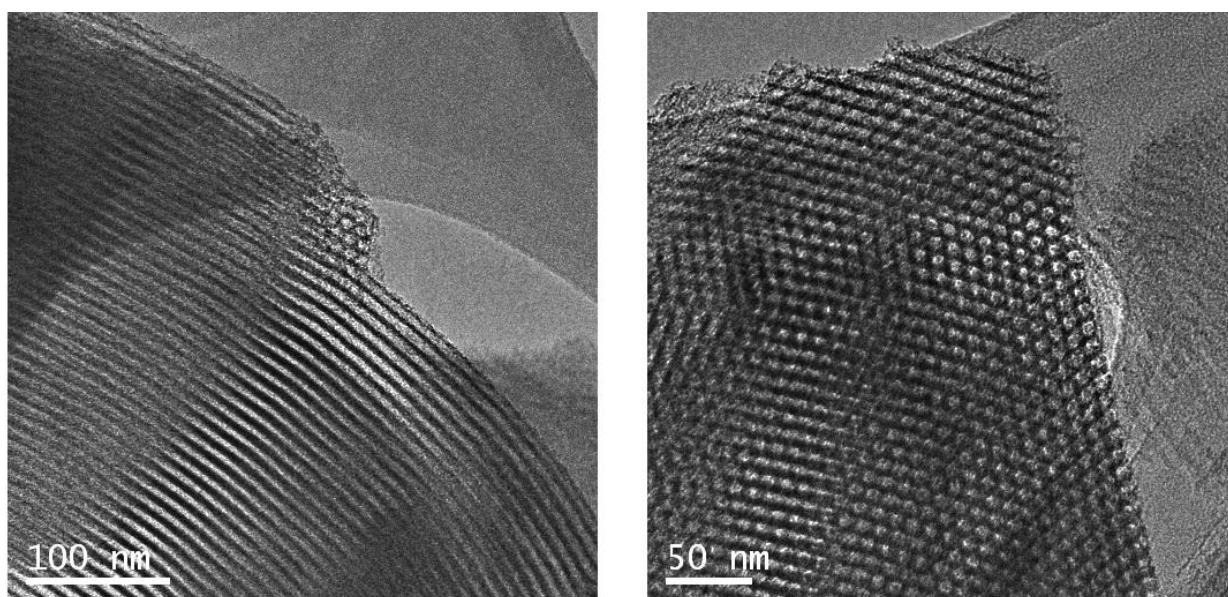
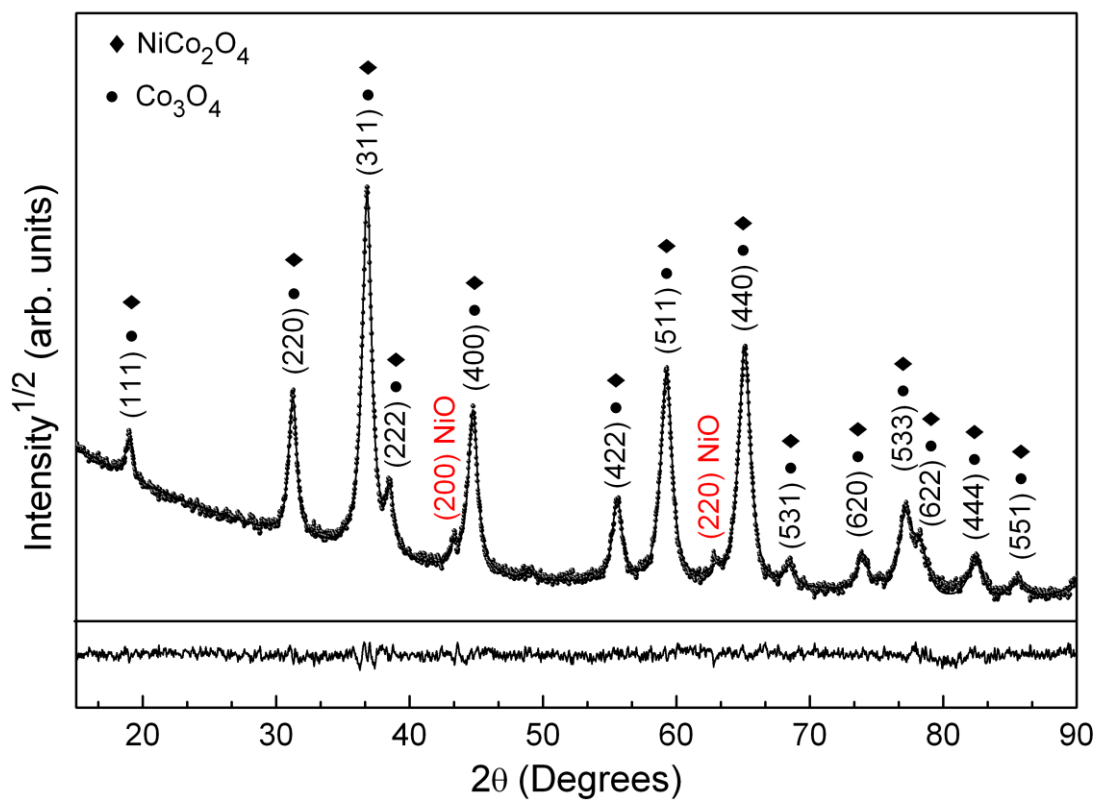**Fig. S1.** TEM images of the SBA-15 silica template.

Fig. S2. Experimental pattern (●), Rietveld fitting (solid line) and Rietveld difference between the original and computed spectra (at the bottom) of the powder obtained from 0.25:1 Ni(II):Co(II) molar ratio of the metal precursors. The peaks at $2\theta = 43.4°$ and $63.0°$ correspond to the (200) and (220) reflections, respectively of the NiO phase (JCPDF 73-1519). Goodness of fitting, $R_w = 9.27$.
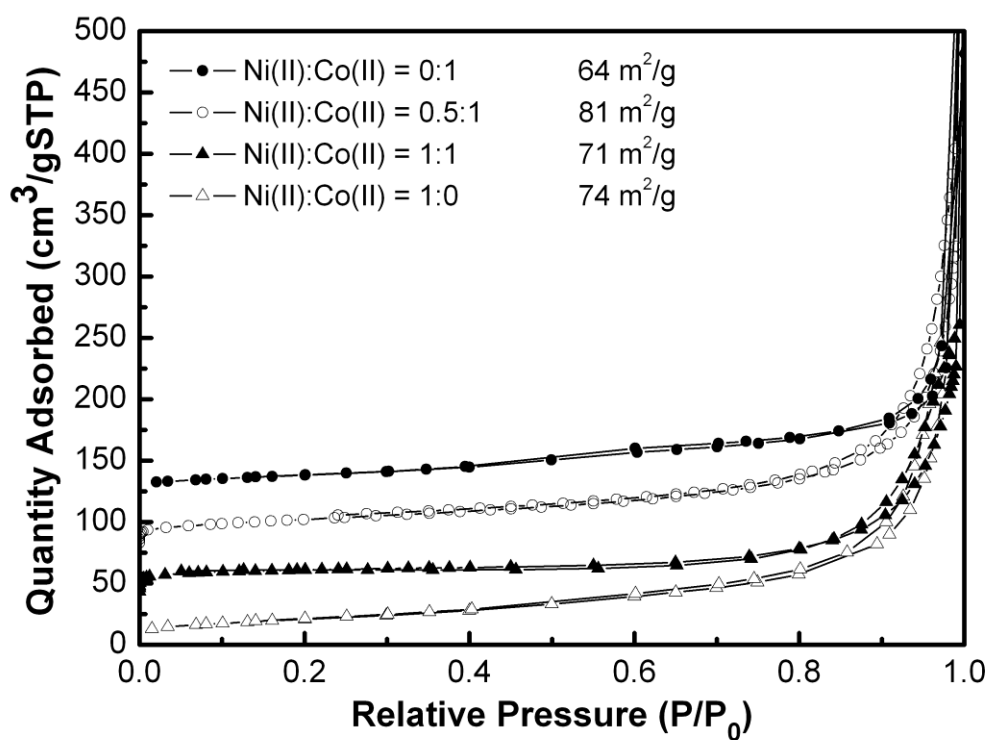
Fig. S3. Typical N$_2$ adsoption-desorption isotherms and corresponding BET areas of the powders obtained form the indicated Ni(II):Co(II) ratios.